The Thesis Committee for Joshua Clark Neitzel
certifies that this is the approved version of the following Thesis:

Application of Quantum Force Computations for Raman Spectroscopy and Molecular Dynamics

Committee:

James R. Chelikowsky, Supervisor

Alexander A. Demkov

Application of Quantum Force Computations for Raman Spectroscopy and Molecular Dynamics

by

Joshua Clark Neitzel

DISSERTATION

Presented to the Faculty of the Graduate School of

The University of Texas at Austin

in Partial Fulfillment

of the Requirements

for the Degree of

MASTER OF ARTS

THE UNIVERSITY OF TEXAS AT AUSTIN

August 2019

Acknowledgments

First and foremost I want to identify the direct and invaluable role that others provided for work in this thesis.

The results presented in chapter 2 are based on a pre-print manuscript titled *B-P codopant effects on Raman spectra of Si nanocrystals using real space pseudopotentials* by Joshua Neitzel and James R. Chelikowsky. J. Neitzel performed the calculations, edited the research code, and performed data analysis. J. R. Chelikowsky suggested and supervised the project. Both authors participated in discussions of the data and in writing the manuscript.

Chapter 3 contains work in preparation for submission with authors Joshua Neitzel, Charles Lena, Grady Schofeld, and James R. Chelikowsky. J. Neitzel performed molecular dynamics calculations and manuscript writing. C. Lena performed molecular dynamics calculations code development, and assisted in manuscript writing. G. Schofeld set up initial software framework and consulting role. J.R. Chelikowsky supervised the project.

More generally I would like to thank the entire Chelikowsky research group. They have been excellent collaborators and coworkers through my entire time at UT Austin.

A special thanks goes to Matt Ervin and Robert Hoelscher for doing all the underappreciated tasks without which your respective departments would

fall apart.

Thanks to the various roommates who never complained about me forgetting to clean the bathroom when they had every right to.

Thanks to my loving parents for their unwavering support through everything.

And thanks to Kathleen Telling for making this entire process more enjoyable and everything else along with it.

Application of Quantum Force Computations for Raman Spectroscopy and Molecular Dynamics

Publication No. _____

Joshua Clark Neitzel, M.A.
The University of Texas at Austin, 2019

Supervisor: James R. Chelikowsky

Electronic structure calculations have undergone incredible advancement in the past century. Using modern methods and supercomputing infrastructure we are now able to compute precise electron behavior in a variety of large and complex systems. However, these computations are only as good as their applications. To further these computations we consider two applications of efficient force calculations using first principles density functional theory.

We compute the vibrational and Raman spectra for B-doped, P-doped, and B-P codoped Si nanocrystals using real-space pseudopotentials constructed within density functional theory. An experimental peak in the Raman spectra near 650 cm^{-1} observed in codoped nanocrystals can be best explained by the presence of B-P bonds, which are located near the surface of the nanocrystal. We propose that the spectral details of this peak are related to quantum confinement and the breaking of local symmetry associated with the phonon modes involving dopant bonds.

We also illustrate an improved method for calculation of nonlocal contributions to interatomic forces is used to perform molecular dynamics simulations. This method results from the real space density functional theory Hamiltonian utilizing a high order Gaussian integration scheme in real space. The efficacy of this method is demonstrated through molecular dynamics simulations of an O_2 molecule and a benzene molecule. Our method improves convergence of dynamic variables including stability and vibrational frequency.

Table of Contents

List of Tables

List of Figures

Chapter 1

Introduction

1.1 Background

1.1.1 Kohn-Sham Equation

Electronic structure problems are quantum problems where one solves for the wave functions and energy levels of electrons in an external potential. As is typical for particles on a quantum mechanical scale, the wave functions and energies are determined by the Schrödinger equation (1.1).

$$\hat{H}\psi = E\psi \tag{1.1}$$

For electrons in molecular matter it is often safe to treat contributions from atomic nuclei as a fixed external potential, allowing the Hamiltonian operator ($\hat{H}$) to be treated in three terms (1.2).

$$\hat{H} = \hat{T} + \hat{V}_{Ion} + \hat{V}_{Hartree} \tag{1.2}$$

Here $\hat{T}$ is the kinetic energy operator for the electrons, $\hat{V}_{Ion}$ is the external potential applied to the electrons from the atomic ions cores, and $\hat{V}_{Hartree}$ is the Coulombic interaction between electrons. In a system with n electrons at positions $\mathbf{r}_i$ and N atomic nuclei at positions $\mathbf{R}_I$ and respective nuclear

charges Z_I we can write down each of these terms (1.3, 1.4, 1.5):

$$\hat{T} = -\frac{\hbar^2}{2m_e}\sum_{i=1}^{n}\nabla_i^2 \tag{1.3}$$

$$\hat{V}_{Ion} = -\sum_{i=1}^{n}\sum_{I=1}^{N}\frac{Z_I e^2}{|\mathbf{r}_i - \mathbf{R}_I|} \tag{1.4}$$

$$\hat{V}_{Hartree} = -\sum_{i=1}^{n}\sum_{j=i+1}^{n}\frac{e^2}{|\mathbf{r}_i - \mathbf{r}_j|} \tag{1.5}$$

While this problem can be solved for small numbers of electrons, it quickly becomes intractable as the dimensionality of the problem scales with the number of electrons. Even small molecules and simple materials require approximations to become solvable. Because the electronic structure of large and complex molecular structures is of great interest to physical chemists and condensed matter physicists alike, the solutions of these equations are important. In finding these solutions, the issue is thus not whether to approximate, but instead which approximations works best to produce useful results.

Hohenberg, Kohn, and Sham demonstrated a key fact that enables one such approximation. [1, 2] While the multi-electron eigenfunction (ψ) has a dimensionality that scales linearly with the number of electrons involved, any observable of this wavefunction must also be contained in a charge density (ρ) with a dimensionality that is fixed and independent of the number of electrons. They also showed that the total energy of the system can be written as a functional of this density ($E[\rho]$) and that the charge density that minimizes this

energy functional must be the ground state charge density of the corresponding Schrödinger equation.

To apply this density functional theory (DFT) practically, the most common approach is to treat the system as a set of non-interacting wave functions (ϕ) that each approximate the wave function of an individual electron. The charge density can be related to these wave functions as follows (1.6).

$$\rho(\mathbf{r}) = \sum_{i=1}^{n} |\phi_i(\mathbf{r})|^2 \tag{1.6}$$

Kinetic energy (T in 1.7) and external potential terms (E_{Ion} in 1.8) are easily written in this formulation.

$$T = -\frac{\hbar^2}{2m_e} \sum_{i=1}^{n} \langle \phi_i | \nabla^2 | \phi_i \rangle \tag{1.7}$$

$$E_{Ion}[\rho] = \int V_{Ion}(\mathbf{r}) \rho(\mathbf{r}) \mathrm{d}\mathbf{r} \tag{1.8}$$

However, the electron-electron interactions are harder to replicate owing to the existence of many-body quantum mechanical interactions. The Coulomb interaction can still be recreated fully in the single particle model using the simple electrostatic form (1.9).

$$E_{Hartree}[\rho] = \frac{1}{2} \int \frac{\rho(\mathbf{r}_1)\rho(\mathbf{r}_2)}{|\mathbf{r}_1 - \mathbf{r}_2|} \mathrm{d}\mathbf{r}_1 \mathrm{d}\mathbf{r}_2 \tag{1.9}$$

The many electron exchange and correlation interactions require the introduction of an abstract $E_{XC}[\rho]$ to capture the appropriate behavior. The variational principle then allows us to use functional derivatives to give appropriate

single particle energies (1.10).

$$V_\alpha(\mathbf{r}) = \frac{\delta E_\alpha[\rho]}{\delta \rho} \tag{1.10}$$

This gives us all the terms to write the Kohn-Sham equation (1.11).

$$\left(\frac{-\hbar^2\nabla^2}{2m_e} + V_{Ion}(\mathbf{r}) + V_{Hartree}(\mathbf{r}) + V_{XC}(\mathbf{r})\right)\phi_i(\mathbf{r}) = E_i\phi_i(\mathbf{r}) \tag{1.11}$$

This still leaves us with a bootstrapping problem. Because writing equation 1.11 requires some input value for ρ and then produces a new ρ via equation 1.6, there is a circular dependence. In practice, this is solved using a self-consistent field (SCF) approach. Some initial value of ρ is guessed, a new one is computed, then the new value is fed back into the equation repeatedly until our metric of interest, such as ρ has converged to within an acceptable tolerance.

A central problem in this description is the difficulty of producing the exchange-correlation functional $E_{XC}[\rho]$. As no method exists for deriving a completely general form for this functional, such functionals are usually produced by generalizing and extrapolating from known limiting cases. For instance, in the case of a homogeneous electron guess we know exchange and correlation effects are purely local. This leads to the simple and surprisingly effective class of exchange-correlation functionals that obey the local density approximation (LDA) in which the functional is, as the name suggests, based entirely on local values of the electron density. Because the exchange energy of the homogeneous electron gas can be found analytically it is precisely this

functional that is often used in the LDA. Unfortunately, there is no similarly general analytic form for the correlation energy so numerical approaches, such as the frequently employed quantum Monte Carlo results from Ceperley and Alder [3], are required. This version of LDA has proved highly resilient and generalizes well even to systems that appear to be nothing like the homogeneous electron gas from which it is derived. In producing the results shown later in this work, this form of the LDA has proven sufficient. Occasional test comparisons between exchange-correlation functionals have shown no significant difference between the results produced by commonly employed functionals for the studied systems.

1.1.2 Pseudopotentials

While the Kohn-Sham equation makes the electronic structure problem computationally tractable, further approximations can greatly increase its efficiency while preserving its accuracy. One of the most valuable such approximations stems from the observation that core electrons present great computational difficulty while contributing little to the physically and chemically important details of electronic structure.

The computational difficulty of these electrons ultimately stems from the singularity of the Coulomb potential at the center of an atomic nuclei. Treating this singularity computationally requires dealing with the problem both at impractically small length scales and across multiple magnitudes of energy. Electrons at this drastically different energy scale present numeri-

cal difficulties in solving the problem while contributing little to the relevant physics or chemistry of the system.

To solve all of these problems while also taking advantage of the chemical inertness of the core electrons, we treat them as a fixed external factor along with their associated nuclear cores as a "pseudopotential." This approach provides the added benefit of reducing computational load by reducing the number of electrons included in the Kohn-Sham eqaution. Because the Kohn-Sham equation is an eigenvalue problem with a number of eigenvalues proportional to the number of electrons present, we expect the $\mathcal{O}(n^3)$ scaling common for numerical eigensolvers. This means that, especially for large atoms (sodium or heavier) consisting of majority core electrons, this approach can cut computational time dramatically.

The goal of these pseudotentials is to construct them such that no changes to the wave function exist outside of the atomic core. This core region is defined by a cutoff radius r_c. A pseudo-wave function can then be constructed to be smooth and well-behaved within this region while matching the all-electron valence wavefunction outside r_c. Pseudopotentials constructed from these pseudo-wave functions by are obtained by inverting the Kohn-Sham equation.

Proper behavior under numerical operations is usually ensured by fixing curvature of the pseudo-wave function as zero at the origin. An additional constraint is provided in ensuring that normality is not violated, in other words the integral across all space of the pseudo-wave function squared must integrate

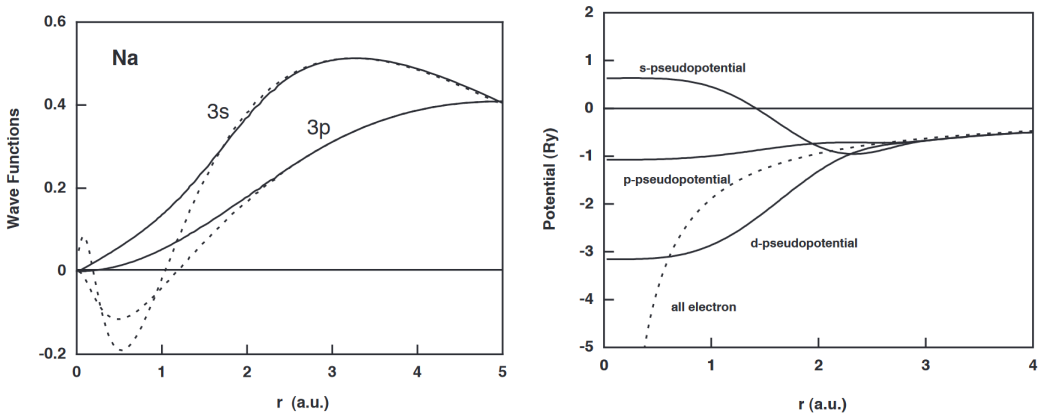

Figure 1.1: An example psuedo-wave function for sodium (left) and the associated pseudopotential (right). The dotted lines represent the all electron wave function and potential, which can be observed overlapping the pseudo functions above the r_c. [4]

to unity. Continuity of the wave function and some number of derivatives at r_c provide additional constraints.

In the following work we use the formulation given by Troullier and Martins to construct our pseudopotentials. [5] Inside r_c this pseudo-wafe funcion ϕ is of the form given in equations 1.12 and 1.13.

$$\phi_p(r) = r^l e^{p(r)} \tag{1.12}$$

$$p(r) = \sum_{i=1}^{6} c_{2i} r^{2i} \tag{1.13}$$

Coefficients in equation 1.13 are found by solving the previously described constraints and l indexes the angular momentum number of the associated all electron orbital.

1.1.3 Real Space Calculations

The approach to DFT described thus far has been predicated on the assumption that the problem would eventually be solved numerically via computational tools. In any such scheme the wave function and electron density must be represented in a finite form that can be stored within a computer.

One common approach is to represent these functions in a plane-wave basis where each function is treated as a linear combination of plane waves. The basis size is limited in this method by only considering wave vectors of magnitude below some cutoff value.

The plane wave approach has distinct advantages, such as the ability to write the kinetic energy as a purely diagonal term. It is also a natural basis for periodic systems.

Plane waves also have distinct disadvantages. One is their inherently global nature. This can be observed in the need to use numerical Fourier transforms to translate between plane wave and spatial coordinates. Such transforms result in high communications costs when attempting parallelized computations. [4] Additionally, the inherent periodicity of this basis means that when solving for the properties of isolated and confined systems a large amount of vacuum space is necessary to minimize the effects of the built in periodic images of the electron density.

In this work, we represent wave functions on a real space grid. While skewed or adaptive grids could be used for this purpose, a non-adaptive cubic

grid is much easier to implement. In this representation the Hamiltonian is constructed as a matrix where the Hartree and exchange-correlation energies are purely diagonal. Kinetic energy is included by applying a small nearly diagonal finite differencing stencil such as the one prescribed by Fornberg. [6]

The ionic pseudopotential contributions are the least diagonal terms as their construction via inversion of the Kohn-Sham equation results in more complex matrix forms. However these terms can still be efficiently represented using the form introduced by Kleinman and Bylander. [7]

$$V_{Ion} = \sum_{a} V_{Local,a} + \sum_{a,l,m} c_{a,l,m} U_{a,l,m} U^{T}_{a,l,m} \tag{1.14}$$

In this form of pseudopotential V, a sums over atomic nuclei while l and m are the usual quantum numbers associated with atomic orbitals and U is a sparse matrix constructed analogously to previously described pseudopotential operators. Because the non-locality in these pseudopotentials is limited to regions of atomic cores the Hamiltonian remains overall very sparse and strongly diagonal, and thus can be stored through implicit means. [8]

1.1.4 Chebyshev Filtering

As the Kohn-Sham equation is an eigenvalue equation, being able to efficiently diagonalize matrices is important to solving the electronic structure problem in the way that has been outlined. Such algorithms typically scale as $\mathcal{O}(n^3)$ where n is the size of the matrix, though a variety of methods improve on this in specific cases.

For real space representations of the Kohn-Sham equation, the problem centers over a specific range of energy eigenvalues of the sparse matrix. To specify this range Zhou *et al.* proposed the method of Chebyshev-Filtered Subspace Iteration (CheFSI). [9] In this method direct diagonalization is only performed in the first step of the SCF loop. Each subsequent step employs a Chebyshev filtering step in which a polynomial of the matrix is used to target a specific energy range of eigenvalues. The new eigenfunctions are then computed through ortho-normalization. In this way the matrix and basis evolve with the SCF process rather than having to start over entirely for each iteration, all while targeting the desired eigenvalues for accelerated performance. This approach has been shown to be competitive with other highly efficient eigensolvers designed for sparse matrices. [10]

1.2 Applications of Force Calculations using Density Functional Theory

Simulation and computation are only as good as the data you can extract from them. In this thesis, we focus specifically on applications involving the extraction of forces on atomic cores. These calculations all stem from the classical definition of force as a derivative of energy. 1.15

$$\mathbf{F}_I = -\nabla_I E \tag{1.15}$$

While forces could be calculated this way from finite differencing, atomic

positions are an input variable to DFT and thus computing forces this way would require multiple full SCF loops for each atom in the system. Such an approach would be very computationally expensive.

Instead, forces can be extracted from a single SCF loop using the Hellmann-Feynman theorem. [11] In this approach we take advantage of this theorem to write the force in terms of a derivative of the Hamiltonian and compute it directly from the Kohn-Sham energy.

We use this force calculation to two very different ends. In the first we use this approach to simulate the results of Raman spectroscopy. In Raman spectroscopy vibrational modes of a molecule are excited through electromagnetic radiation and differences between input and output photon energies are used to extract phonon energies of the molecule. In order to predict these exact phonon energies the eigenvalues of the Hessian matrix must be computed, which means finding the Hessian matrix from quantum forces.

Unfortunately the Hessian matrix is slightly more complex than just the forces of the system. Instead, it is the second derivative of the energy with respect to atomic position and the Hellmann-Feynman equation only works up to first derivatives. So, in order to compute this matrix we apply the earlier mentioned finite differencing approach to generate the derivatives of the forces. Generating the Hessian matrix in this way provides vibrational details of molecular structures which is required in the Raman spectroscopy analysis in chapter two.

The second application of these forces requires both efficient performance and an consistent accuracy from them. Molecular Dynamics (MD) relies heavily on force calculations in order to apply Newton's second law while integrating systems in time. In chapter three we consider applications of DFT force calculations to MD by applying a recently developed higher-order method to generate accurate and efficient forces.

Chapter 2

BP Codopant Effects on Raman Spectra in Si Nanocrystals

2.1 Introduction

Silicon nanocrystals (Si-NCs) are important in the design of devices with room-temperature luminescence, optoelectronic properties, and biomedical applications. [12–18] Additionally, Si-NCs serve as a paradigm for understanding quantum confinement in semiconductors. [19–21] The properties of Si-NCs are sensitive to nanocrystal size owing to the role of quantum confinement. These properties can be measured using a combination of Raman spectroscopy, x-ray diffraction, and transmission electron microscopy. [22–26] Light emission from electrically stimulated Si-NCs in particular has garnered attention. [27,28] Raman in particular is used as a tool to distinguish nanocrystal size, with the main peak redshifting and broadening as size increases. Both phenomenological models and pseudopotential based DFT calculations have offered explanations for this mechanism. [21, 29–32]

Our analysis of this system focuses on the introduction of dopants and codopants. Dopants play a vital role in tuning existing properties of semiconductors, such as the band gap and carrier density. [33–35] Boron and phos-

phorous have been used extensively as p- and n- type dopants respectively for both bulk Si and Si-NCs. The introduction of these dopants controls experimentally measurable values. For instance, P doped Si-NC has been shown both experimentally and in DFT calculations to produce a noticeable redshift in the main Raman peak. [36]

Creating B and P doped Si-NCs of smaller and smaller size pushes the limits of solid solubility. [20, 37] However, systems with both of these dopants in combination reflect a reduced formation energy and allow for significantly higher dopant rates. [38,39] These colloidal particles have been realized experimentally and are of interest for the tunability of their luminescence energy and increased dispersibility in polar liquids. Raman spectroscopy is used as one of the primary methods of analysis for these systems, with peaks demonstrating known relationships between dopant type and concentration. [40–42]

Doping nanocrystalline Si introduces structural degrees of freedom, which complicates any discussion. Whereas the surface to volume ratio is vanishingly small in bulk, the ratio is substantial in Si-NCs and requires one to consider the difference between surface and interior dopants for nanocrystals. [43] This variation of dopant location significantly affects the electrical and optical properties of nanocrystals. [44–46] The characterization of dopant location is a key step in understanding the properties of these structures through direct modeling of the Raman spectroscopy.

Computational models of NC allow for precision and detail when modeling Raman spectroscopy in this manner. The inherently small scale of NCs

allow for full DFT simulations of the entire system and the direct comparison of the calculated Raman spectra to experiment. This computational work serves not only to verify experimentally observed and expected trends, but to explore new methods of structural determination and the associated physical properties. For instance, previous studies were able to determine the effect of changing size and dopant location for P in Si-NCs. They also determined that these changes were caused not by changes to the phonon structure but by dopants altering the polarizability of the NC. [36]

2.2 Methodology

Our computational work is based on pseudopotentials constructed within density functional theory. We incoproprate norm-conserving Troullier-Martins pseudopotentials as implemented in our earlier work. [5,36,47] Our calculations were performed using the PARSEC software package, which solves the Kohn-Sham problem in real space. [4,8,48,49] Exchange correlation corrections were made using the local density approximation. [5] The PARSEC code was designed for nanocrystalline systems. The Kohn-Sham equation is discretized on a cubic lattice seperated by 0.3 Bohr. This discretization enables substantially reduced global communications and improved parallelism for large atomic systems owing to localized interactions in contrast to methods using a plane wave basis. Real space approaches also allow for non-periodic boundary conditions, reducing the necessary vacuum space radius for convergence. [4, 8, 48, 49] For our calculations, we use a 5 Bohr minimum vacuum radius around each clus-

ter. Convergence in PARSEC is accelerated through the use of a subspace filter. This filtering method uses Chebyshev polynomials to filter the matrix subspace to speed convergence after computing an approximate eigenvalue solution for the first self-consistency step, finalizing convergence after energy is self-consistent within 10^{-5} Ry. [9, 10]

We calculate the vibrational eigenmodes and eigenfrequencies by computing the force constants to generate a dynamical matrix. Equilibrium positions are establihed by minimizing energy with respect to atom coordinates until residual forces are reduced to under 10^{-4} Ry/a.u. (1 a.u.=0.5292Å). Force constants are then computed by displacing each atom position from equilibrium in 0.005 a.u. steps along each cartesian direction, computing force values, then calculating a simple centered difference. The matrix generated from these values is then directly diagonalized to generate eigenvalue frequencies and eigenvectors for the associated phonon modes. [50]

The nonresonant Raman spectra can then be calculated from the vibrational modes using Plazcek's polarizability approximation. Under this approximation, the nth vibrational eigenmode, ν^n, contributes to the Raman tensor in proportion to the change in dielectric susceptability, χ,

$$\alpha_{ij}^{n} = \sum_{Ik} \frac{\partial \chi_{ij}}{\partial r_{Ik}} \frac{\nu_{Ik}^{n}}{\sqrt{M_I}}. \tag{2.1}$$

Here, I labels the atoms, k specifies the Cartesian components, r represents position and M represent that atomic mass. The partial derivative is computed via finite differencing as a second derivative of force with respect to electric

field. [51, 52] The Raman cross section averaged over nanocrystal orientations is computed as the following function of frequency,

$$\frac{d\sigma(\omega)}{d\Omega} \sum_n (45\alpha'^2_n + 7\beta'^2_n)\delta(\omega - \omega_n), \tag{2.2}$$

where $\alpha'_n = \frac{1}{3}(\alpha^n_{xx} + \alpha^n_{yy} + \alpha^n_{zz})$ is the mean of the polarizability derivative and $\beta'_n = \sqrt{\frac{1}{2}[(\alpha^n_{xx} - \alpha^n_{yy})^2 + (\alpha^n_{yy} - \alpha^n_{zz})^2 + (\alpha^n_{zz} - \alpha^n_{xx})^2 + 6(\alpha^n_{xy}{}^2 + \alpha^n_{yz}{}^2 + \alpha^n_{zx}{}^2)]}$ is the anisotropy contribution of the polarizability derivative. [53, 54]

2.3 Results

We considered seven Si nanocrystal structures with 87 core atoms and different quantities and mixtures of B and P dopants. An additional pair of 147 core atom clusters were also constructed after identifying targets for detailed study. Each cluster is constructed by building a segment of Si crystal up to a fixed maximum radius then capping any unbonded Si with H atoms. Appropriate core Si atoms are replaced with dopants when necessary then each structure is individually relaxed until residual forces are within acceptable tolerances (10^{-4} Ry/a.u.). These two sizes have proven themselves before as large enough to approximate nanostructure properties while remaining small enough to be efficiently calculated. [21, 36]

In Fig. 2.1 we present the calculated vibrational density of states (VDOS) for each nanocrystal, excluding contributions from the passivating H atoms, which correspond to higher vibrational modes. Our results show very little variation between the different systems. For the entire region from around 100

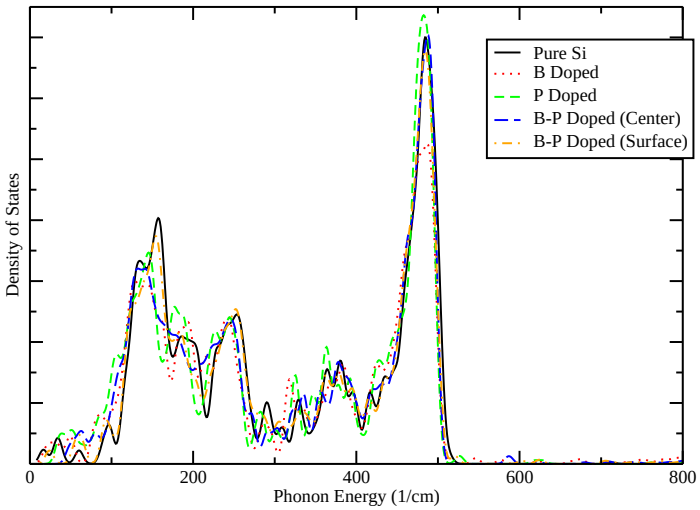

Figure 2.1: Vibrational density of states of various 87 core atom Si-NCs. The dense phonon structure changes little with the variations in dopant location, indicating that the selection effect of the polarizability matrix is key for determining any changes in the Raman spectra between structures. The plot also demonstrates the relative sparseness of phonons above 500 cm^{-1}, the region in which individual phonons are more likely to have outsize influence on the final Raman spectra.

to 500 cm^{-1} the DOS is dense and largely homogonous for the various systems, meaning differences in Raman spectra within these ranges are likely to come from changes in the Raman cross section. For phonons in sparser region the picture becomes more complicated due to the outsize influence a single phonon in these regions can have.

For the Raman spectra we separate the seven structures into two cases for clarity, those with and without B-P bonds. We do this with the expectation

that the peak located in experimental measurements around 625 cm^{-1} will be associated with the B-P bonding. [42]

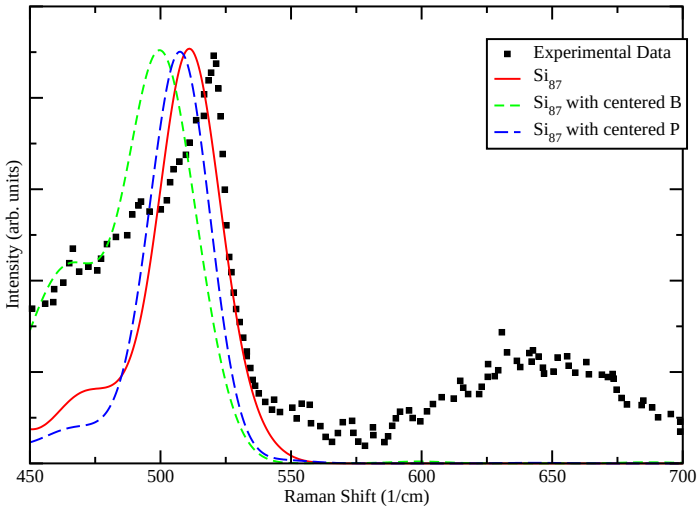

Figure 2.2: Simulated raman spectra for 87 core atom Si-NCs without codoping. Experimental results for BP codoped nanocrystals are shown as a basis for comparison. [42] Note that the simulated spectra show nothing of the experimental peak around 650 cm^{-1}. This demonstrates that single dopant effects are unlikely to produce this feature. However, the B doping does reproduce some of the peak broadening effect around 450 cm^{-1}.

The structures without the B-P bond, as expected, lack this characteristic (Fig. 2.2). This feature does appear in the Raman spectra for structures with B-P bonding, both in the previously shown structures as well as additional studies in larger nanocrystals consisting of 147 core Si atoms (Fig. 2.3). This result supports an interpretation that the experimentally detected feature arises from BP codoping of the Si nanocrystal, as is also supported by

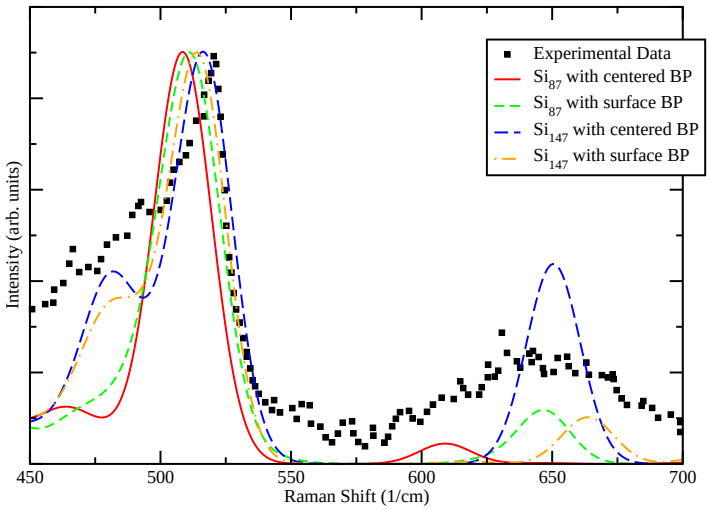

Figure 2.3: Simulated raman spectra for 87 and 147 core atom Si-NCs with codoping. Experimental results for BP codoped nanocrystals are shown as a basis for comparison. [42] Note that the simulated spectra for these systems all show features aorund the 650 cm^{-1} peak. This demonstrates that this experimentally observed feature is linked to the codopants as expected. In particular, the 147 core atom Si-NCs matches up well with the peak locations, with the surface and centered structures combining to match the broad peak. The pronounced size of the 147 core atom centered structure is due to a twofold degeneracy in the phonons associated with this peak.

X-ray photoelectron spectroscopic studies. [42]

Additionally, the four B-P codopant systems allow us to correlate the position of the codopant peak to the dopant location and nanocrystal. In Table 2.1, these four data points indicate two trends. As nanocrystal size increases the peak location blueshifts. Additionally, as the dopants are moved closer to the surface the peak location also blueshifts.

Number of Core Atoms	Centered Dopants	Surface Dopants
87	587	625
147	628	642

Table 2.1: Values provided in cm^{-1}. Two clear trends are apparent: peak location increases in wavelengths as the dopants move toward the surface and when the nanocrystal increases in size.

A key advantage of our simulations, compared to experiment, is the ability to directly examine the vibrational modes associated with this secondary B-P peak. The composition of these modes confirms that these modes are primarily tied to vibration of the B and P dopant atoms, with some additional minor vibration of Si and H atoms that neighbor the codopants. Of the two dopants, the B moves atom's displacement vector is significantly larger due to lighter mass and weaker bonds compared to the P.

Examination of these simulations also demonstrates that any changes in the codopant peak must come from changes in the phonon structure and not from changes in the Raman cross section. Whereas studies on purely P-doped Si-NC showed significant changes in the way the Raman cross section interacted with phonons, for these systems the sparseness of phonon modes was a much more significant factor than the Raman cross section. [36] Instead of a large number of modes being selected by the cross section, instead only a few particular modes associated with the codopant bonds exist. All of these modes were Raman sensitive, meaning the exact behavior of these small number of phonons is highly significant in the final Raman spectra.

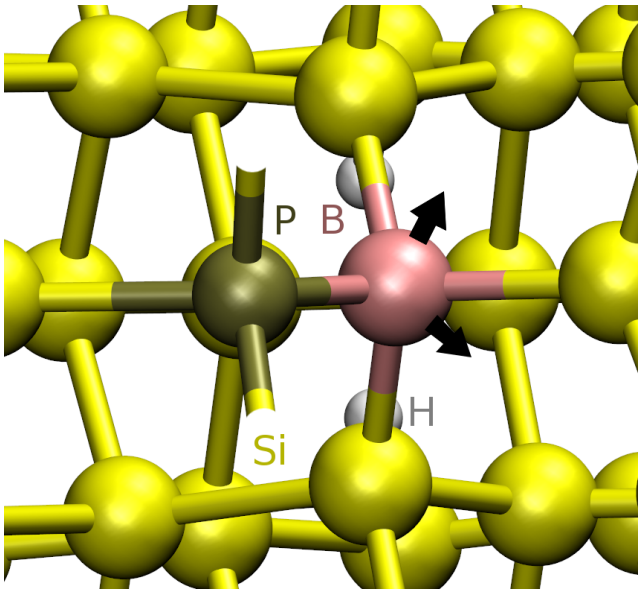

Figure 2.4: Raman activated phonon modes associated with the codopant peak for a 147 core atom Si-NC with centered codopants. The arrows demonstrate the direction of motion of two degenerate modes with the arrow length being proportional to the size of the atom movement. Movement of all atoms besides the B is negligible for these modes. The symmetry of these phonons can easily be observed here, with the motion of the B atom in both cases existing in the plane perpendicular to the BP bond.

By comparing the modes where codopants are centered within the NC versus the case where they are near the surface, we notice a notable change in the vibrational modes. Whereas the centered modes consist entirely of vibrations where the B and P move perpendicular or parallel to the BP bond direction (Fig. 2.4), the surface doped structures contain more skewed angles between the modes and the bonds (Fig. 2.5). This is to be expected because the force constants of the dopants are affected by the local structure of the NC and locations closer to the center of a nanocrystal are significantly higher in

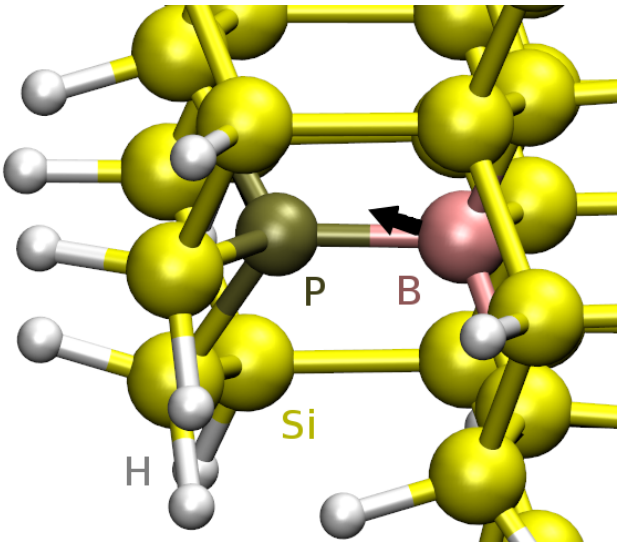

Figure 2.5: Raman activated phonon modes associated with the codopant peak for a 147 core atom Si-NC with surface codopants. The arrows demonstrate the direction of motion of the mode with the arrow length being proportional to the size of the atom movement. Movement of all atoms besides the B is negligible for this phonon. The direction of movement is heavily skewed at an irregular angle compared to the bonding structure due to the lack of local symmetry near the surface.

symmetry than those closer to the surface. The blueshift of the peak associated with these atoms is best explained an increased effective spring constant related to the symmetry breaking of the phonon mode. In both figures, a small shift (20 cm^{-1}) was made to align the main spectral feature of the computations with experiment.

The blueshift associated with increasing NC size can be attributed to a reduction of contributions from the "under-coordination" bonding associated with the surface. This is has also been observed in intrinsic Si NC. Since the NC surface is capped with a reduced number of Si-Si bonds, the overall

surface structure is softer when compared to a fully saturated bulk crystal. This surface effect is reduced as the NC increases in size resulting in the Raman peak blueshift. [21]

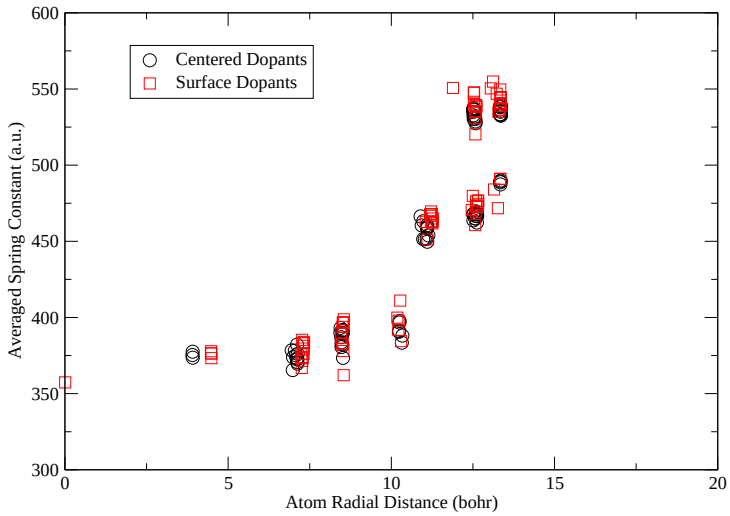

Figure 2.6: Effective spring constants for each Si in the codoped 87 atom nanocrystal. Spring constants are plotted as a function of radial distanceof the Si atom. Each spring constant value is calculated by averaging the diagonal elements of the Hessian matrix for each atom.

We can directly examine how bond stiffness is associated with atomic location in the nanocrystal. From our previous work, the Si-Si bond lengths are known to be different in the interior of a NC compared to the surface. For example, Si-Si bond lengths decrease near the surface of Si NCs. [21] However, bond length alone does not provide enough information to quantify how vibrational properties are affected. We can quantify an approximate "local spring

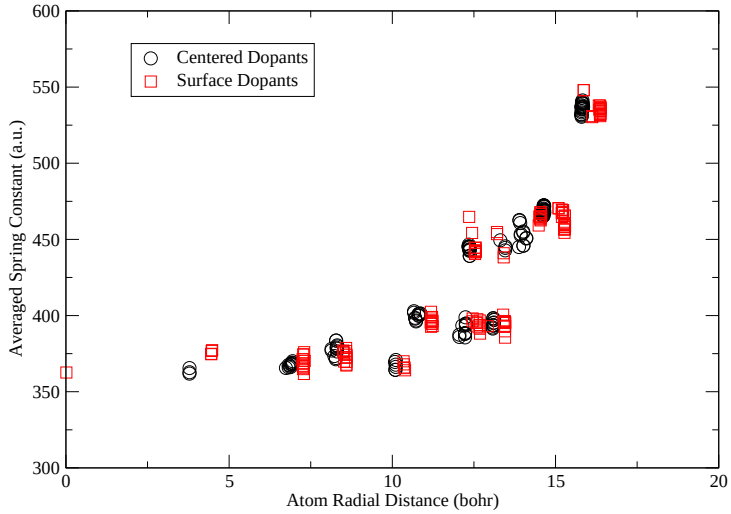

Figure 2.7: Effective spring constants for each Si in the codoped 147 atom nanocrystal. Spring constants are plotted as a function of radial distance of the Si atom. Each spring constant value is calculated by averaging the diagonal elements of the Hessian matrix for each atom.

constant" for each atom from the Hessian matrix. This value is simply the second derivative of energy with respect to change in position of a single atom, averaged over each direction. When plotted for Si atoms as a function of radial position of each atom it provides a clear trend (Figs. 2.6, 2.7). The local spring constant increases for bonds closer to the surface. Similar trends are observed for the B dopants. The effective spring constant for the P dopants shows little difference between cases, but remains significantly larger and stiffer than those associated with the other atoms. The increased flexibility of the Si-Si bonds near the surface allows the B-P bond in the codoped structure to strengthen

compared to the B-P bond in the interior. Consistent with our earlier work, the strengthened bonding increases the energy of the vibrational modes associated with the movement of B in the codopant, resulting in a corresponding blueshift of Raman spectral features associated with these modes.

2.4 Summary

We examined the vibration properties and Raman spectra of P-doped, B-doped, and BP-codoped Si nanocrystals and compared these spectra to experimentally measured spectra. The distinguishing feature in the experimental measurement is that in addition to the Si peak around 525 cm^{-1} there is a smaller secondary peak around 650 cm^{-1}. We simulate spectra for a variety of B and P doped Si-NC structures and find that the simulated spectra with B-P bonded BP codopants replicate this 650 cm^{-1} peak.

In contrast to previous work on purely P-doped Si-NC, we find that the location of this codopant peak is highly dependant on the phonons involved and has little dependence on the Raman cross-section. This effect is due to the sparse occupancy of phonons in this region meaning the experimental peaks are dominated by the exact character of the few phonons that exist in this range. Such a direct relationship between phonon behavior and Raman spectroscopy results invites new experiments and measurements in order to use Raman spectroscopy to directly probe phonon character in this and similar materials.

We find that this 650 cm^{-1} secondary peak location changes with respect to NC size and codopant location. The peak blueshifts with increasing

NC size. It also blueshifts as the dopants move closer to the surface. These blueshifts both correlate to changes in the phonons associated with the Raman peaks. These phonons represent modes associated with the vibration of the B atom within the BP codoped bond, each affected by the differing detail of the structure in which it is embedded. The overall shift in these phonon energies is best described by two different effects. Increasing NC size results in increased overall coordination, resulting in increased stiffness of the NC and the blueshift with larger sizes. Readjustment and strengthening of codopant bonds near the surface results in copants closer to the surface having stronger bonds and a similar blueshift in the vibrational modes. These two effects provide a mechanism for future use in experimental results that could allow for enhanced distinction of structure using Raman spectroscopy.

Chapter 3

Molecular Dynamics using Higher Order Forces

This chapter contains work in preparation for submission with authors Joshua Neitzel, Charles Lena, Grady Schofeld, and James R. Chelikowsky. J. Neitzel performed molecular dynamics calculations and manuscript writing. C. Lena performed molecular dynamics calculations code development, and assisted in manuscript writing. G. Schofeld set up initial software framework and consulting role. J.R. Chelikowsky supervised the project.

3.1 Introduction

One popular application for computational simulation of atomic scale materials is molecular dynamics. In molecular dynamics, the properties of a material are found by numerically integrating a the equations of motion for the constituent particles. Such simulations have proven useful for understanding the statistical and out of equilibrium behavior of systems such as DNA, [55] quantum dots, [56] and cyclic hydrocarbons. [57] While such simulations are often performed using coarse models for atomic behavior these models are a result of limited computational ability and not an ideal circumstance. Bringing

DFT to bear more fully on these systems would provide greater insight and more accurate representation to MD simulation as opposed to purely classical forces.

The largest barrier to incorporating DFT into MD is computational expense. MD calculations often require long running times to gather significant data about a system and runs for thousands of timesteps are common. As such, using detailed *ab initio* techniques such as DFT that themselves require significant computational complexity at each step can require great computing resources.

Advances such as Chebyshev filtering can ease some of this computational expense. [10, 58] However, the use of DFT for these applications is still limited by the need for precise and consistent force calculations. Small discrepancies cannot be tolerated in MD simulation due to the fact that small errors compound quickly through repeated integration steps. Ensuring enough accuracy for this purpose requires high levels of convergence, which means higher energy cutoffs for plane waves or finer grid spacings for real space methods, which increases computational expense for either method.

Recent improvements in accuracy of force calculation while avoiding a finer grid spacing has been done using high order integration techniques. [59] These techniques have been to compute more accurate and consistent forces at lower grid spacing as compared to previous real space techniques. Implementing, proving, and applying this method for MD using DFT would make *ab initio* detail available in MD simulation for practical applications. This

application promises a new level of precision and incorporation of quantum mechanical behavior in MD calculations.

3.2 Computational Details

Our calculatons were performed using a branch of the real-space pseudopotential package, PARSEC [4, 48], which solves the Kohn-Sham equation self-consistently on a uniform grid. This code uses a higher order finite difference expression for the kinetic energy operator [9]. Pseudopotentials were constructed using the Troullier-Martins prescription [5]. Convergence of the self-consistency cycle is accelerated by using damped Chebyshev polynomial filtering subspace iteration. [9, 60]. The discretization scheme is a uniform cubic grid in real space, with variable grid spacing, h, always listed in a.u. of values between 0.2 and 0.4. Confined boundary conditions were used, and wave functions were constrained to zero outside a cubic domain with a vacuum space of 5 a.u. from the outermost atoms.

3.3 Results

For all tested molecules and parameters the high order integration scheme (HO) conserved energy better than the traditional low order method (LO). Energy conservation was tested by examining total energy evolution for the O_2 and C_6H_6 molecules across different values of the grid spacing parameter (h). In each case we excite vibrational modes of the molecule, impart no initial kinetic energy, then integrate forward in time with timesteps of 1.0 fs.

The simplest such test was for an O_2 molecule with an excited vibrational mode along the direction of the bond. A few example trajectories of such excitations are plotted in Fig. 3.1 and show both the desired energy evolution, the periodic bounded evolution observed for $h = 0.3$, and an undesirable and unreliable evolution, the irregular unbounded case for LO with $h = 0.4$. These evolutions are also the first piece of evidence for the relative strength of the HO scheme, as the irregular evolution only occured in any of our test cases for the LO algorithm.

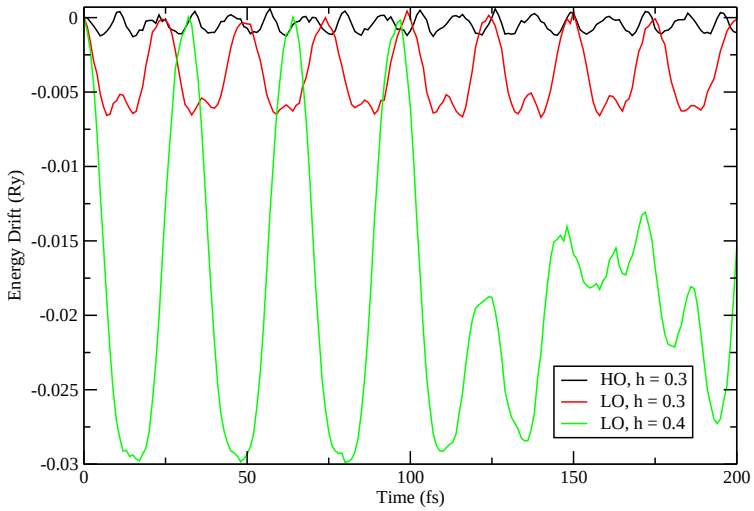

Figure 3.1: Example total energy drifts over time for MD simulation of the O_2 dimer. Normal, bounded oscillations are shown for both the HO and LO oscillations at $h = 0.3$. Additionally, a case of irregular oscillations is shown for comparison in the LO scheme with $h = 0.4$.

Plotting the absolute magnitude of these oscillations as a fraction of the

total kinetic energy oscillations for various grid spacings, see Fig. 3.2, provides further proof of the strength of the HO scheme. For every grid spacing value where regular oscillations were measured, the fractional size of the oscillations was smaller for the HO implementation. Using 10% as an upper limit on the maximum energy deviation the HO scheme was able to surpass this mark at $h = 0.3$ where the LO scheme requires $h = 0.2$.

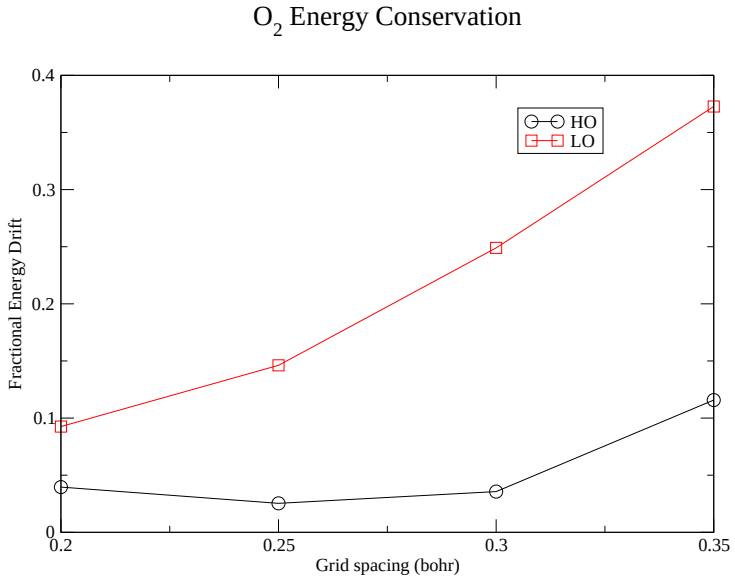

Figure 3.2: Magnitude of total energy oscillations as a fraction of kinetic energy oscillations for the O_2 dimer.

Performing a similar analysis for benzene, C_6H_6, demonstrates the strength of the HO scheme for larger and more complex molecules. For these molecular dynamics computations, we intentionally excited a limited number of longitudinal modes of the molecule to simplify normal mode analyis. Energy

drift over time is shown in Fig. 3.3 with $h = 0.3$, the value for which we see the most benefit from the HO integration. This case shows substantial reductions in the magnitude of energy drift for the HO approach compared to the LO.

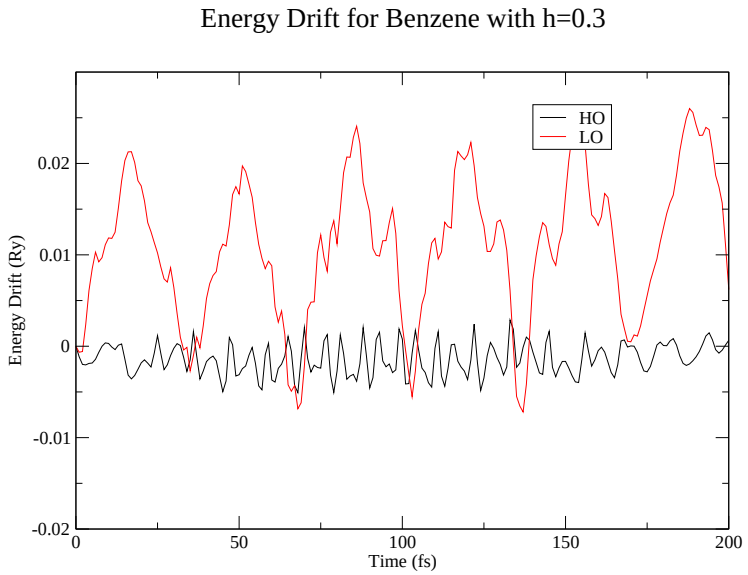

Figure 3.3: Total energy evolution of C_6H_6 over time for both high-order (HO) and low-order (LO) algorithms at a grid spacing of $h = 0.3$ a.u.

As an additional test of our algorithms, we consider the convergence of the oscillation period, τ, of the O_2 dimer. (Fig. 3.4) In this case one observes clearly that the HO method converges faster than the LO method, reaching essentially stable values at $h = 0.3$ instead of the still unconverged values for the LO method at $h = 0.2$. That is, the dynamic values of the LO integration method remain highly variable on grid spacing up to very fine values, whereas molecular dynamics using the HO method are consistent up to a larger grid

spacing. It is also worth noting that while this converged frequency is significantly lower (20%) than the ideal harmonic frequency computed for the same molecule, this is easily explained by the anharmonicity of the high amplitude initial conditions.

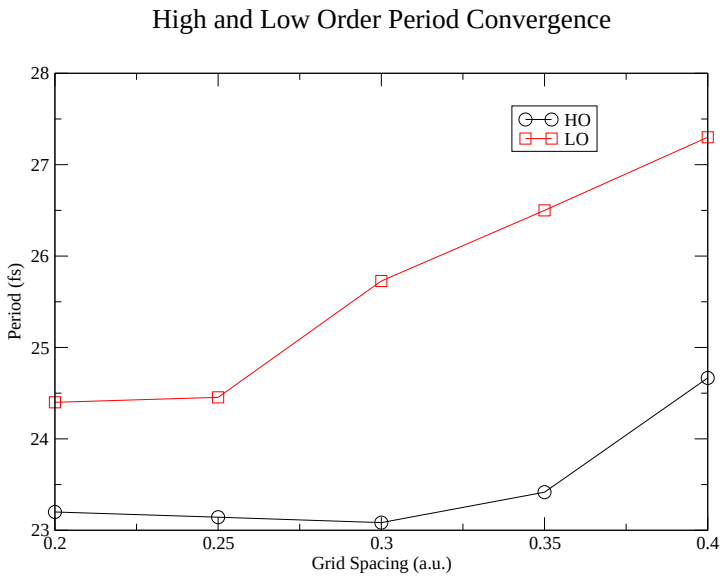

Figure 3.4: Oscillation period for O_2 as a function of grid spacing, h, for both HO and LO methods.

Bibliography

[1] Pierre Hohenberg and Walter Kohn. Inhomogeneous electron gas. *Physical review*, 136(3B):B864, 1964.

[2] Walter Kohn and Lu Jeu Sham. Self-consistent equations including exchange and correlation effects. *Physical review*, 140(4A):A1133, 1965.

[3] David M Ceperley and BJ Alder. Ground state of the electron gas by a stochastic method. *Physical Review Letters*, 45(7):566, 1980.

[4] James R Chelikowsky. The pseudopotential-density functional method applied to nanostructures. *Journal of Physics D: Applied Physics*, 33(8):R33, 2000.

[5] Norman Troullier and José Luís Martins. Efficient pseudopotentials for plane-wave calculations. *Physical review B*, 43(3):1993, 1991.

[6] Bengt Fornberg. Generation of finite difference formulas on arbitrarily spaced grids. *Mathematics of computation*, 51(184):699–706, 1988.

[7] Leonard Kleinman and DM Bylander. Efficacious form for model pseudopotentials. *Physical Review Letters*, 48(20):1425, 1982.

[8] James R Chelikowsky, N Troullier, and Yousef Saad. Finite-difference-pseudopotential method: Electronic structure calculations without a basis. *Physical review letters*, 72(8):1240, 1994.

[9] Yunkai Zhou, Yousef Saad, Murilo L Tiago, and James R Chelikowsky. Parallel self-consistent-field calculations via chebyshev-filtered subspace acceleration. *Physical Review E*, 74(6):066704, 2006.

[10] KH Khoo, Minjug Kim, Grady Schofield, and James R Chelikowsky. Ab initio molecular dynamics simulations using a chebyshev-filtered subspace iteration technique. *Physical Review B*, 82(6):064201, 2010.

[11] Richard Phillips Feynman. Forces in molecules. *Physical Review*, 56(4):340, 1939.

[12] Shoji Furukawa and Tatsuro Miyasato. Three-dimensional quantum well effects in ultrafine silicon particles. *Japanese journal of applied physics*, 27(11A):L2207, 1988.

[13] Dmitri V Talapin and Christopher B Murray. PbSe nanocrystal solids for n-and p-channel thin film field-effect transistors. *Science*, 310(5745):86–89, 2005.

[14] Jeffrey J Urban, Dmitri V Talapin, Elena V Shevchenko, Cherie R Kagan, and Christopher B Murray. Synergism in binary nanocrystal superlattices leads to enhanced p-type conductivity in self-assembled PbTe/Ag_2Te thin films. *Nature materials*, 6(2):115, 2007.

[15] Ilan Gur, Neil A Fromer, Michael L Geier, and A Paul Alivisatos. Air-stable all-inorganic nanocrystal solar cells processed from solution. *Science*, 310(5747):462–465, 2005.

[16] Steven A McDonald, Gerasimos Konstantatos, Shiguo Zhang, Paul W Cyr, Ethan JD Klem, Larissa Levina, and Edward H Sargent. Solution-processed PbS quantum dot infrared photodetectors and photovoltaics. *Nature materials*, 4(2):138, 2005.

[17] X Michalet, FF Pinaud, LA Bentolila, JM Tsay, SJJL Doose, JJ Li, G Sundaresan, AM Wu, SS Gambhir, and S Weiss. Quantum dots for live cells, in vivo imaging, and diagnostics. *science*, 307(5709):538–544, 2005.

[18] Weibo Cai, Dong-Woon Shin, Kai Chen, Olivier Gheysens, Qizhen Cao, Shan X Wang, Sanjiv S Gambhir, and Xiaoyuan Chen. Peptide-labeled near-infrared quantum dots for imaging tumor vasculature in living subjects. *Nano letters*, 6(4):669–676, 2006.

[19] Igor Vasiliev, Serdar Öğüt, and James R Chelikowsky. Ab initio absorption spectra and optical gaps in nanocrystalline silicon. *Physical Review Letters*, 86(9):1813, 2001.

[20] T-L Chan, Murilo L Tiago, Efthimios Kaxiras, and James R Chelikowsky. Size limits on doping phosphorus into silicon nanocrystals. *Nano letters*, 8(2):596–600, 2008.

[21] KH Khoo, AT Zayak, H Kwak, and James R Chelikowsky. First-principles study of confinement effects on the Raman spectra of Si nanocrystals. *Physical review letters*, 105(11):115504, 2010.

[22] Z Iqbal and S Veprek. Raman scattering from hydrogenated microcrystalline and amorphous silicon. *Journal of Physics C: Solid State Physics*, 15(2):377, 1982.

[23] Ch Ossadnik, S Vepřek, and I Gregora. Applicability of Raman scattering for the characterization of nanocrystalline silicon. *Thin Solid Films*, 337(1-2):148–151, 1999.

[24] Hua Xia, YL He, LC Wang, W Zhang, XN Liu, XK Zhang, D Feng, and Howard E Jackson. Phonon mode study of Si nanocrystals using micro-Raman spectroscopy. *Journal of Applied Physics*, 78(11):6705–6708, 1995.

[25] Minoru Fujii, Yoshihiko Kanzawa, Shinji Hayashi, and Keiichi Yamamoto. Raman scattering from acoustic phonons confined in Si nanocrystals. *Physical Review B*, 54(12):R8373, 1996.

[26] Giuseppe Faraci, Santo Gibilisco, Paola Russo, Agata R Pennisi, and Salvo La Rosa. Modified Raman confinement model for Si nanocrystals. *Physical Review B*, 73(3):033307, 2006.

[27] Liang-Sheng Liao, Xi-Mao Bao, Ning-Sheng Li, Xiang-Qin Zheng, and Nai-Ben Min. Visible electroluminescence from Si+-implanted SiO_2

films thermally grown on crystalline Si. *Solid state communications*, 97(12):1039–1042, 1996.

[28] Mingxiang Wang, Xinfan Huang, Jun Xu, Wei Li, Zhiguo Liu, and Kunji Chen. Observation of the size-dependent blueshifted electroluminescence from nanocrystalline Si fabricated by KrF excimer laser annealing of hydrogenated amorphous silicon/amorphous-SiN x: H superlattices. *Applied physics letters*, 72(6):722–724, 1998.

[29] H Richter, ZP Wang, and L Ley. The one phonon Raman spectrum in microcrystalline silicon. *Solid State Communications*, 39(5):625–629, 1981.

[30] Jian Zi, H Büscher, C Falter, W Ludwig, Kaiming Zhang, and Xide Xie. Raman shifts in Si nanocrystals. *Applied Physics Letters*, 69(2):200–202, 1996.

[31] Jian Zi, Kaiming Zhang, and Xide Xie. Comparison of models for Raman spectra of si nanocrystals. *Physical Review B*, 55(15):9263, 1997.

[32] Wei Cheng and Shang-Fen Ren. Calculations on the size effects of Raman intensities of silicon quantum dots. *Physical Review B*, 65(20):205305, 2002.

[33] David J Norris, Alexander L Efros, and Steven C Erwin. Doped nanocrystals. *Science*, 319(5871):1776–1779, 2008.

[34] Steven C Erwin, Lijun Zu, Michael I Haftel, Alexander L Efros, Thomas A Kennedy, and David J Norris. Doping semiconductor nanocrystals. *Nature*, 436(7047):91, 2005.

[35] David Mocatta, Guy Cohen, Jonathan Schattner, Oded Millo, Eran Rabani, and Uri Banin. Heavily doped semiconductor nanocrystal quantum dots. *Science*, 332(6025):77–81, 2011.

[36] KH Khoo and James R Chelikowsky. First-principles study of vibrational modes and Raman spectra in P-doped Si nanocrystals. *Physical Review B*, 89(19):195309, 2014.

[37] Shu Zhou, Xiaodong Pi, Zhenyi Ni, Qingbin Luan, Yingying Jiang, Chuanhong Jin, Tomohiro Nozaki, and Deren Yang. Boron-and phosphorus-hyperdoped silicon nanocrystals. *Particle & Particle Systems Characterization*, 32(2):213–221, 2015.

[38] Stefano Ossicini, Elena Degoli, F Iori, E Luppi, Rita Magri, G Cantele, F Trani, and D Ninno. Simultaneously B-and P-doped silicon nanoclusters: Formation energies and electronic properties. *Applied Physics Letters*, 87(17):173120, 2005.

[39] F Iori and S Ossicini. Effects of simultaneous doping with boron and phosphorous on the structural, electronic and optical properties of silicon nanostructures. *Physica E: Low-dimensional Systems and Nanostructures*, 41(6):939–946, 2009.

[40] Federico Iori, Elena Degoli, Rita Magri, Ivan Marri, G Cantele, D Ninno, F Trani, O Pulci, and Stefano Ossicini. Engineering silicon nanocrystals: theoretical study of the effect of codoping with boron and phosphorus. *Physical Review B*, 76(8):085302, 2007.

[41] Hiroshi Sugimoto, Minoru Fujii, Kenji Imakita, Shinji Hayashi, and Kensuke Akamatsu. Codoping n-and p-type impurities in colloidal silicon nanocrystals: Controlling luminescence energy from below bulk band gap to visible range. *The Journal of Physical Chemistry C*, 117(22):11850–11857, 2013.

[42] Minoru Fujii, Hiroshi Sugimoto, Masataka Hasegawa, and Kenji Imakita. Silicon nanocrystals with high boron and phosphorus concentration hydrophilic shell—Raman scattering and x-ray photoelectron spectroscopic studies. *Journal of Applied Physics*, 115(8):084301, 2014.

[43] Xiaobo Chen, Xiaodong Pi, and Deren Yang. Critical role of dopant location for P-doped Si nanocrystals. *The Journal of Physical Chemistry C*, 115(3):661–666, 2010.

[44] XD Pi, R Gresback, RW Liptak, SA Campbell, and U Kortshagen. Doping efficiency, dopant location, and oxidation of Si nanocrystals. *Applied Physics Letters*, 92(12):123102, 2008.

[45] Minoru Fujii, Yasuhiro Yamaguchi, Yuji Takase, Keiichi Ninomiya, and Shinji Hayashi. Control of photoluminescence properties of Si nanocrys-

tals by simultaneously doping n-and p-type impurities. *Applied Physics Letters*, 85(7):1158–1160, 2004.

[46] Minoru Fujii, Shinji Hayashi, and Keiichi Yamamoto. Photoluminescence from B-doped Si nanocrystals. *Journal of Applied Physics*, 83(12):7953–7957, 1998.

[47] J.-H. Eom, T.-L. Chan and J.R. Chelikowsky. Vacancies and B doping in Si nanocrystals. *Solid State. Commun.*, 150:130, 2010.

[48] Leeor Kronik, Adi Makmal, Murilo L Tiago, MMG Alemany, Manish Jain, Xiangyang Huang, Yousef Saad, and James R Chelikowsky. Parsec–the pseudopotential algorithm for real-space electronic structure calculations: recent advances and novel applications to nano-structures. *physica status solidi (b)*, 243(5):1063–1079, 2006.

[49] Jiaxin Han, Murilo L Tiago, T-L Chan, and James R Chelikowsky. Real space method for the electronic structure of one-dimensional periodic systems. *The Journal of chemical physics*, 129(14):144109, 2008.

[50] K. Parlinski, Z. Q. Li, and Y. Kawazoe. First-principles determination of the soft mode in cubic ZrO_2. *Phys. Rev. Lett.*, 78:4063–4066, May 1997.

[51] Dirk Porezag and Mark R. Pederson. Infrared intensities and Raman-scattering activities within density-functional theory. *Phys. Rev. B*, 54:7830–7836, Sep 1996.

[52] P Umari and Alfredo Pasquarello. Infrared and Raman spectra of disordered materials from first principles. *Diamond and related materials*, 14(8):1255–1261, 2005.

[53] Edgar Bright Wilson, John Courtney Decius, and Paul C Cross. *Molecular vibrations: the theory of infrared and Raman vibrational spectra*. Courier Corporation, 1955.

[54] Derek Steele. *Theory of vibrational spectroscopy*, volume 8. Saunders Limited., 1971.

[55] Alberto Pérez, F Javier Luque, and Modesto Orozco. Frontiers in molecular dynamics simulations of DNA. *Accounts of chemical research*, 45(2):196–205, 2011.

[56] Run Long and Oleg V Prezhdo. Ab initio nonadiabatic molecular dynamics of the ultrafast electron injection from a pbse quantum dot into the tio2 surface. *Journal of the American Chemical Society*, 133(47):19240–19249, 2011.

[57] J Postma, Ronnie Hoekstra, AGGM Tielens, and Thomas Schlathölter. A molecular dynamics study on slow ion interactions with the polycyclic aromatic hydrocarbon molecule anthracene. *The Astrophysical Journal*, 783(1):61, 2014.

[58] KH Khoo, T-L Chan, M Kim, and James R Chelikowsky. Ab initio molecular dynamics simulations of molten Al 1-x Si x alloys. *Physical*

Review B, 84(21):214203, 2011.

[59] N Scott Bobbitt, Grady Schofield, Charles Lena, and James R Chelikowsky. High order forces and nonlocal operators in a Kohn–Sham Hamiltonian. *Physical Chemistry Chemical Physics*, 17(47):31542–31549, 2015.

[60] Grady Schofield, James R Chelikowsky, and Yousef Saad. A spectrum slicing method for the Kohn–Sham problem. *Computer Physics Communications*, 183(3):497–505, 2012.